JOURNAL OF GEOPHYSICAL RESEARCH, VOL. 112, A07309, doi:10.1029/2006JA012222, 2007

Cassini Ion and Neutral Mass Spectrometer data in Titan's upper atmosphere and exosphere: Observation of a suprathermal corona

V. De La Haye,[1] J. H. Waite Jr.,[1] R. E. Johnson,[2] R. V. Yelle,[3] T. E. Cravens,[4] J. G. Luhmann,[5] W. T. Kasprzak,[6] D. A. Gell,[1] B. Magee,[1] F. Leblanc,[7] M. Michael,[8] S. Jurac,[9] and I. P. Robertson[4]

Received 12 December 2006; revised 29 January 2007; accepted 3 April 2007; published 27 July 2007.

[1] The neutral nitrogen and methane measurements made by Ion and Neutral Mass Spectrometer during Cassini flybys T_A, T_B, and T_5 in Titan's upper atmosphere and exosphere are presented. Large horizontal variations are observed in the total density, recorded to be twice as large during T_A as during T_5. Comparison between the atmospheric and exospheric data show evidence for the presence of a significant population of suprathermal molecules. Using a diffusion model to simultaneously fit the N_2 and CH_4 density profiles below 1500 km, the atmospheric structure parameters are determined, taking into account recent changes in the calibration parameters. The best fits are obtained for isothermal profiles with values 152.8 ± 4.6 K for T_A, 149.0 ± 9.2 K for T_B, and 157.4 ± 4.9 K for T_5, suggesting a temperature ≃5 K warmer at night than at dusk, a trend opposite to that determined by solar-driven models. Using standard exospheric theory and a Maxwellian exobase distribution, a temperature of 20 to 70 K higher would be necessary to fit the T_A, T_B, and egress-T_5 data above 1500 km. The suprathermal component of the corona was fit with various exobase energy distributions, using a method based on the Liouville theorem. This gave a density of suprathermals at the exobase of $4.4 \pm 5.1 \times 10^5$ cm^{-3} and $1.1 \pm 0.9 \times 10^5$ cm^{-3}, and an energy deposition rate at the exobase of $1.1 \pm 0.9 \times 10^2$ eV cm^{-3} s^{-1} and $3.9 \pm 3.5 \times 10^1$ eV cm^{-3} s^{-1} for the hot N_2 and CH_4 populations, respectively. The energy deposition rate allowed us to roughly estimate escape rates for nitrogen of $\simeq 7.7 \pm 7.1 \times 10^7$ N cm^{-2} s^{-1} and for methane of $\simeq 2.8 \pm 2.1 \times 10^7$ CH_4 cm^{-2} s^{-1}. Interestingly, no suprathermal component was observed in the ingress-T_5 data.

Citation: De La Haye, V., et al. (2007), Cassini Ion and Neutral Mass Spectrometer data in Titan's upper atmosphere and exosphere: Observation of a suprathermal corona, *J. Geophys. Res.*, *112*, A07309, doi:10.1029/2006JA012222.

1. Introduction and Background

1.1. Cassini INMS Data: Flybys T_A, T_B, T_5, and T_7

[2] The Cassini Ion and Neutral Mass Spectrometer has two ion sources: a closed source to measure nonreactive neutral species, composed of a spherical antechamber with an entrance orifice connected to an ionization region, and an open source to measure reactive neutral and ion species [*Waite et al.*, 2005a]. The first in situ mass spectrometry measurements of Titan's upper atmosphere were acquired by INMS in the closed source mode during T_A, the first close Titan flyby of Cassini [*Waite et al.*, 2005b]. At closest approach (1174.0 km), measurements were made for the following neutrals: molecular nitrogen (with a density of 10^9 cm^{-3}), methane (with a mixing ratio of 2.2×10^{-2}), molecular hydrogen (with a mixing ratio of 4.4×10^{-3}), acetylene, ethylene, ethane, and C_3H_4. Other species such as C_3H_8, C_4H_2, HCN, HC_3N, C_6H_6, and C_2N_2 were identified at less than 5 ppm. In addition, large spatial scale (≃180 km) and large-amplitude (≃10 K) atmospheric waves were observed between 1174 and 1500 km [*Müller-Wodarg et al.*, 2006].

[3] An analysis of the N_2, CH_4, and H_2 vertical profiles for T_A allowed *Yelle et al.* [2006] to determine the atmospheric structure of Titan's upper atmosphere in the region of the flyby. The temperature in the upper atmosphere was

[1] Southwest Research Institute, San Antonio, Texas, USA.
[2] Astronomy Department, University of Virginia, Charlottesville, Virginia, USA.
[3] Lunar and Planetary Laboratory, University of Arizona, Tucson, Arizona, USA.
[4] Department of Physics and Astronomy, University of Kansas, Lawrence, Kansas, USA.
[5] Space Sciences Laboratory, University of California, Berkeley, California, USA.
[6] NASA Goddard Space Flight Center, Greenbelt, Maryland, USA.
[7] Service d'Aéronomie du CNRS/IPSL, Paris, France.
[8] Civil Engineering, Indian Institute of Technology, Kanpur, India.
[9] Center for Space Research, Massachusetts Institute of Technology, Cambridge, Massachusetts, USA.

0148-0227/07/2006JA012222$09.00

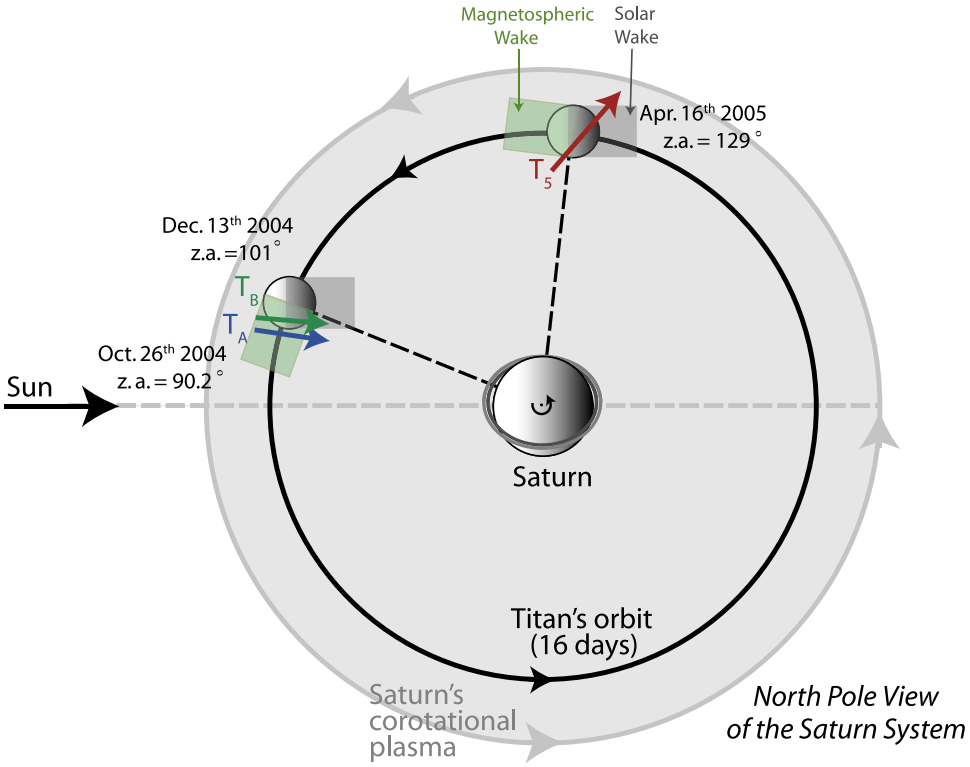

Figure 1. Visualization of the T_A, T_B, and T_5 flyby trajectories with respect to Saturn and to the Sun. The parameters denoted z.a. represent the zenith angles for each flyby at closest approach.

found to be fit best with an isothermal profile of 149 ± 3 K, in good agreement with the temperature derived after the reanalysis of the UVS Voyager data by *Vervack et al.* 2004], who reported an asymptotic temperature of 152.9 K for the evening terminator and 157.7 K for the morning terminator. *Yelle et al.* [2006] also found that certain combinations of eddy diffusion and upward flux of methane molecules can provide a good match between the models and the INMS CH_4 density profile. Assuming a negligible upward flux of methane, the eddy coefficient was found to be $5^{+3}_{-2} \times 10^9$ cm^2 s^{-1}, a value about one to two orders of magnitude larger than that used by previous photochemical models but directly comparable to the earlier studies of eddy diffusion in Titan's upper atmosphere [*Smith et al.*, 1982; *Strobel et al.*, 1991; *Vervack et al.*, 2004] and to the effective eddy diffusion coefficient calculated by *Müller-Wodarg and Yelle* [2002], which includes the effects of horizontal dynamics. However, when a CH_4 escape flux of 2.2×10^9 cm^{-2} s^{-1}, referred to Titan's surface, was assumed, an eddy coefficient of only 10^7 cm^2 s^{-1} was found sufficient to provide a good fit to the data [*Yelle et al.*, 2006].

[4] Following T_A, two close flybys of Titan were performed by Cassini at 1197.6 km (T_B) and 1025.2 km (T_5), allowing INMS to return new in situ measurements of the neutrals in Titan's upper atmosphere over an altitude range of several hundreds of kilometers. During flyby T_5, measurements were also performed by INMS in the open source mode, providing the first in situ ionospheric data [*Cravens et al.*, 2006].

[5] The geometry of the T_A, T_B, and T_5 flyby trajectories are presented in Figure 1 with respect to the Saturnian system and solar illumination. As shown on Figure 1, the flybys T_A and T_B occurred in the same configuration with respect to Saturn's magnetosphere and with respect to the Sun: both flybys took place in the magnetospheric wake and crossed the dusk line, heading from the day side toward the night side. The T_5 flyby, however, occurred for different magnetospheric and solar illumination. The Cassini Orbiter passed by Titan on the magnetospheric ram side and remained in the night during most of the T_5 encounter's duration. The flyby trajectories and the Sun's direction are also illustrated in the reference coordinate system of Titan in Figure 2. The direction of the solar radiation remained at approximately the same position during the three flybys, corresponding to a subsolar latitude of about 23° south with respect to Titan's equator. The three flybys occurred in the northern hemisphere. The altitude and latitude variations relevant to the three flybys are plotted in Figure 3 and detailed in Table 1. The T_5 variations in both local time (8.7 hours) and latitude (25°) are about twice as large as those during T_A (3.9 hours, 13°) or T_B (5.3 hours, 10°).

[6] During the closest approaches of T_A and T_5, INMS was pointed in the ram direction (the direction of the spacecraft velocity vector plus the drift velocity of the atmospheric particles). In the closed source mode, the high mach flow penetrating into the small orifice of the closed source leads to a significant dynamic pressure increase inside the spherical antechamber, allowing measurements to be made. This effect falls rapidly to zero when the orifice is not illuminated by the beam (>90°) since the mean free path of the flow is of the order of 10 to 100 m [*Waite et al.*, 2005a]. During the egress portion of T_B, the ram angle was

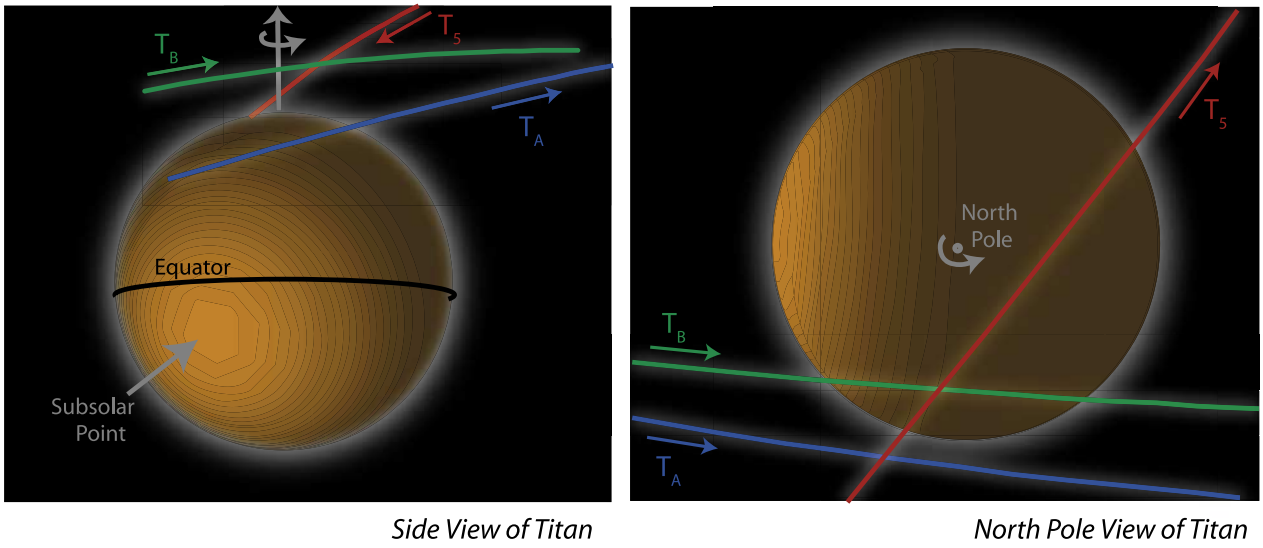

Figure 2. Visualization of the T_A, T_B, and T_5 flyby trajectories with respect to Titan.

in the range 66 to 67°, which allowed the nitrogen and methane density data to be inferred. However, during most of the T_B flyby's ingress portion, the INMS ram angle remained larger than 90°, and the enhancement factor was insufficient for recording appropriate data to analyze the atmospheric structure.

[7] In September 2005, an additional flyby (T_7) was performed by the Cassini orbiter, reaching an altitude of ≃1075 km from Titan's surface. Only a few density measurements were made by INMS during the ingress portion of the flyby at altitudes above 1445 km and at latitudes between 52° and 53° south (Table 1). Although these data points were not numerous enough for analysis of the atmospheric structure and composition, they were the first N_2 and CH_4 in situ measurements of Titan's upper atmosphere in the southern hemisphere.

[8] Since the publication of *Waite et al.* [2005b] and *Yelle et al.* [2006], slight modifications were performed on the calibration factors. In the present article, the N_2 and CH_4 density data recorded by INMS in the closed source mode during Titan flybys T_A, T_B, T_5, and T_7 are presented. The results reported below take into account the calibration

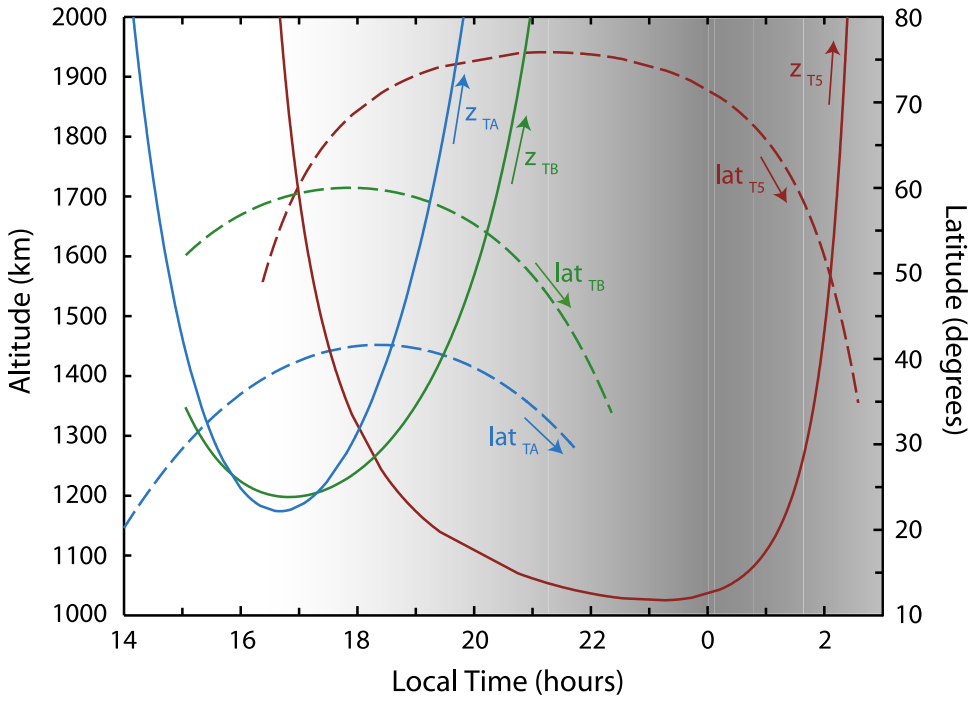

Figure 3. Altitude (solid lines) and latitude (dashed lines) variations during flybys T_A, T_B, and T_5 with respect to Titan's local time.

Table 1. Parameters for the T_A, T_B, T_5, and T_7 Flyby Trajectories

	T_A	T_B	T_5	T_7
Altitude,[a] km	1174.0	1197.6	1025.2	1445
Latitude[a]	38.8°N	59.1°N	73.7°N	53.1°S
Local time,[a] hours	16.7	16.8	0.7	17.4
Zenith angle,[a] deg	90.2	101	129	68.3
Latitudinal variation,[b] deg	13	10	25	1
Local time variation,[b] hours	3.9	5.3	8.7	0.07
INMS ram angle,[b] deg	0.1–23	66–106	0.2–0.4	25–26

[a]Parameters corresponding to closest approach parameters for T_A, T_B, and T_5 and to the lower altitude of the INMS measurements for T_7.
[b]The latitudinal, local time, and ram angle variations are calculated for the portion of the flybys occurring below 1500 km.

changes. Atmospheric structure parameters are derived for flybys T_B and T_5 and are compared to revised atmospheric structure parameters for T_A.

1.2. Exospheric Observations and Models

[9] Prior to the Cassini mission, the observation of airglow emissions by UVS on board Voyager provided the first estimate of 3×10^{26} s^{-1} for the escape rate of nonthermal nitrogen atoms [*Strobel and Shemansky*, 1982]. This value was later revised down to $<10^{25}$ s^{-1} after reconsideration of the N_2 electron impact dissociation rates [*Strobel et al.*, 1992]. *Lammer and Bauer* [1991] described the cooling of hot N atoms produced by electron impact dissociation to the background gas N_2 and suggested that the dissociative recombination of molecular nitrogen ions is a more effective suprathermal neutral production mechanism. Following this work, the role of magnetospheric electron impact was suggested to be less important than direct solar excitation [*Strobel et al.*, 1991; *Gan et al.*, 1992], and N_2^+ was postulated not to be the major ion in Titan's ionosphere [*Keller et al.*, 1992]. This led *Lammer and Bauer* [1993] to consider the effect of atmospheric sputtering by energetic magnetospheric ions (H^+ and N^+) or solar wind protons penetrating Titan's atmosphere. In addition, *Cravens et al.* [1997] showed that photochemistry was an important source of nonthermal neutrals, and *Shematovich* [1998] considered the dissociation and dissociative ionization of molecular nitrogen due to solar UV radiation and energetic photoelectrons. A comprehensive collisional model for the kinetics and dynamics of the hot N and N_2 populations (E > escape energy) in Titan's exobase region was presented by *Shematovich et al.* [2001] and *Shematovich et al.* [2003]. In addition to the production of suprathermal nitrogen atoms and molecules by dissociation and dissociative ionization, *Shematovich et al.* [2003] included sputtering induced by magnetospheric ions H^+ and N^+ and by pick up ions formed from ions thought to be principal ionospheric species near the exobase, $C_2H_5^+$. They reported a total escape rate of $\simeq 3.6 \times 10^{25}$ s^{-1} nitrogen neutrals with comparable rates from dissociation and sputtering.

[10] *Michael et al.* [2005] studied the presence of a sputtered corona (E > 0.1 eV), using a three-dimensional (3-D) Monte Carlo model with improved cross sections for collisional dissociation of N_2. They described the sputtering of atomic and molecular nitrogen from Titan's upper atmosphere and considered sputtering induced by ambient N^+ ions and by molecular pickup ions. They assumed the exobase altitude to be 1500 km and used globally averaged incident fluxes with values 1.1×10^7 cm^{-2} s^{-1} for N^+ and 1.4×10^7 cm^{-2} s^{-1} for N_2^+ and calculated slightly higher escape fluxes than *Shematovich et al.* [2003]: 3.7×10^{26} N s^{-1} as either N or N_2. On the basis of this model, *Michael and Johnson* [2005] examined the influence of sputtering on Titan's upper atmosphere with a 1-D Direct Simulation Monte Carlo model. They found that most of the escaping N_2 and N particles originated from the altitude region around 1400 km, and the temperature profile showed that the ion flux produced an enhanced temperature at the exobase. Using the ion fluxes estimated from *Brecht et al.* [2000], averaged over the full exobase and an initial isothermal thermosphere at T = 155 K, they obtained a $\simeq$7 K increase in temperature at 1600 km. The corresponding density enhancement at 1600 km was $\simeq$30% but is sensitive to the energy spectra of the impacting ions.

[11] In this paper the number density versus altitude profiles of N_2 and CH_4 recorded by INMS during flybys T_A, T_B, and T_5 in Titan's exosphere are presented. These data are examined with respect to the thermal exospheric profiles, modeled by using the temperatures derived from the study of the atmospheric structure at lower altitudes. Estimates for the suprathermal density, escape flux, and energy density are compared to the results of the aforementioned models. The contribution of exothermic ion and neutral chemistry to Titan's corona was studied and compared to the INMS results in a related publication [*De La Haye et al.*, 2007].

2. Titan's Upper Atmosphere

2.1. Data Reduction and Analysis

[12] The data reduction method utilizes the instrument sensitivity and the dissociative patterns resulting from the electron impact of the atmospheric neutrals in the ionization region of the instrument. These parameters were recently reanalyzed by combining information obtained from three sources: the calibration of the flight model (FM) prior to launch, the calibration of the engineering model (EM) after launch, and the NIST spectra. The sensitivities measured with the engineering model were scaled to equate those of the flight model using the N_2 measurements as a transfer standard. In a similar manner, sensitivity values were derived from the NIST data. The methane calibration data were further processed to isolate the signal due to $^{13}CH_4$ from that due to $^{12}CH_4$. Finally, an adjustment of the N_2 cracking pattern was made to insure agreement between the N_2 density inferred from the signal in mass channel 28 and that obtained from the signal in mass channel 14 (after removal of the contribution due to the CH_2 fractionation of methane in the ion source region of the instrument). These changes in the calibration parameters resulted in slight modifications of the INMS composition data since the publication of *Waite et al.* [2005b] and *Yelle et al.* [2006].

[13] In order to extract the atmospheric structure parameters, a multiparameter fit was simultaneously performed on the N_2 and CH_4 density data recorded between closest approach and 1500 km. This fit was performed by using a diffusion model assuming diffusive equilibrium [*Waite et al.*, 2005b]. The transport equation was recast from its more

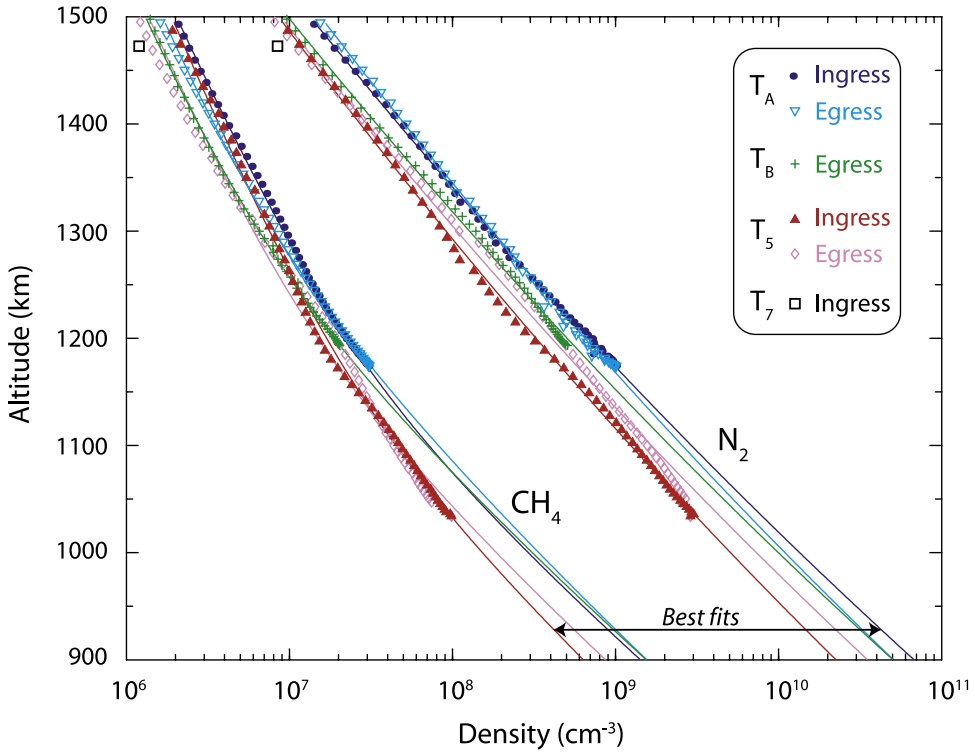

Figure 4. Density data for nitrogen and methane in Titan's upper atmosphere, as returned by INMS during T_A, T_B (egress only), T_5, and T_7 (single data point). The results of the T_A, T_B, and T_5 data fits are represented by solid lines, with a color correspondence to the data.

classic form to adapt to the case where no gas can be defined as a major species [*Yelle et al.*, 2006]:

$$-\tilde{D}_s\left[\frac{1}{n_s}\frac{\partial n_s}{\partial z}+\frac{1}{H_s}+\left(1+\frac{n-n_s}{n}\alpha_T\right)\frac{1}{T}\frac{\partial T}{\partial z}\right] - K\left[\frac{1}{n_s}\frac{\partial n_s}{\partial z}+\frac{1}{H_a}+\frac{1}{T}\frac{\partial T}{\partial z}\right]=0, \quad (1)$$

where T is the neutral temperature, n_s and H_s are the number density and scale height of neutral species s, n and H_a are the atmospheric density and scale height, K is the eddy diffusion coefficient, α_T the thermal diffusion factor, and $\tilde{D}_s$ a modified version of the molecular diffusion coefficient:

$$\tilde{D}_s=\frac{D_s}{1-\frac{n_s}{n}\left(1-\frac{m_s}{m_{\neq s}}\right)}, \quad (2)$$

where m_s is the mean molecular mass of species s, and $m_{\neq s}$ the mean molecular mass of the gas mixture, excluding species s. The numerical method considered for the least squares fit is the conjugated gradient method in multi-dimensions described by *Press et al.* [1996]. The free variables include the temperature (considered isothermal) and a constant eddy coefficient, assuming a negligible upward flux of methane. As mentioned earlier, *Yelle et al.* [2006] showed that the presence of a nonnegligible escape flux of methane would imply a significantly smaller eddy coefficient. However, this issue won't be explored here. The two additional free variables are the N_2 and CH_4 densities at 900 km.

2.2. Results: Titan's Atmospheric Structure

[14] Large density differences were recorded between flybys T_A, T_B, T_5, and T_7 suggesting that horizontal variations in Titan's atmosphere are larger than predicted by models. The nitrogen and methane density data returned by INMS during T_A, T_B (egress), T_5, and T_7 (small portion of ingress) are displayed in Figure 4 and the results of the fits in Table 2. At 1200 km, where data are available for the first three flybys, the density of nitrogen was found to be 6.84 and 6.48 $\times$ 10^8 cm^{-3} for T_A ingress and egress, 5.04 $\times$ 10^8 cm^{-3} for T_B egress, and 3.25 and 4.05 $\times$ 10^8 cm^{-3} for T_5 ingress and egress. The total density recorded by INMS is therefore about twice as large during T_A as during T_5. At 1200 km, the methane mole fractions were found to be 3.23% and 3.45% for T_A ingress and egress, 3.60% for T_B egress, and 4.95% and 3.56% for T_5 ingress and egress, showing that the horizontal variations in the thermosphere involve not only the total density but also the composition.

[15] The T_7 N_2 and CH_4 density data, available above 1470 km only, are the only recorded in the southern hemisphere and are found to be close to the T_5 egress data but significantly smaller than data recorded during T_A. At 1470 km, the nitrogen density was found to be (8.5 $\pm$ 0.1) $\times$ 10^6 cm^{-3}, only about 1.3 times smaller than (1.1 $\pm$ 0.003) $\times$ 10^7 cm^{-3} recorded during T_5 (egress) and about 2.5 times smaller than (2.1 $\pm$ 0.006) $\times$ 10^7 cm^{-3} recorded during T_A (egress); and the methane density was found to be (1.2 $\pm$ 0.03) $\times$ 10^6 cm^{-3}, comparable to (1.5 $\pm$ 0.04) $\times$ 10^6 cm^{-3}

Table 2. Results of the Simultaneous Fit of the INMS N_2 and CH_4 Density Data ($z < 1500$ km)[a]

	T_A	T_B	T_5
	N_2 Density, cm^{-3}		
950 km	$(2.69 \pm 0.32) \times 10^{10}$	$(2.20 \pm 0.64) \times 10^{10}$	$(1.32 \pm 0.26) \times 10^{10}$
1050 km	$(5.78 \pm 0.48) \times 10^{9}$	$(4.56 \pm 0.96) \times 10^{9}$	$(2.96 \pm 0.48) \times 10^{9}$
1200 km	$(6.71 \pm 0.18) \times 10^{8}$	$(5.04 \pm 0.36) \times 10^{8}$	$(3.65 \pm 0.40) \times 10^{8}$
1400 km	$(4.85 \pm 0.21) \times 10^{7}$	$(3.42 \pm 0.42) \times 10^{7}$	$(2.83 \pm 0.13) \times 10^{7}$
	CH_4 Density, cm^{-3}		
950 km	$(7.03 \pm 0.42) \times 10^{8}$	$(6.78 \pm 0.84) \times 10^{8}$	$(3.52 \pm 0.45) \times 10^{8}$
1050 km	$(1.56 \pm 0.12) \times 10^{8}$	$(1.44 \pm 0.24) \times 10^{8}$	$(8.56 \pm 0.53) \times 10^{7}$
1200 km	$(2.29 \pm 0.01) \times 10^{7}$	$(1.88 \pm 0.02) \times 10^{7}$	$(1.57 \pm 0.10) \times 10^{7}$
1400 km	$(3.82 \pm 0.37) \times 10^{6}$	$(2.77 \pm 0.74) \times 10^{6}$	$(3.16 \pm 0.46) \times 10^{6}$
	CH_4 Mixing Ratio		
950 km	$(2.55 \pm 0.45)\%$	$(2.99 \pm 0.90)\%$	$(2.60 \pm 0.18)\%$
1050 km	$(2.63 \pm 0.40)\%$	$(3.05 \pm 0.80)\%$	$(2.81 \pm 0.27)\%$
1200 km	$(3.30 \pm 0.11)\%$	$(3.60 \pm 0.22)\%$	$(4.14 \pm 0.68)\%$
1400 km	$(7.24 \pm 0.94)\%$	$(7.38 \pm 1.88)\%$	$(9.88 \pm 1.69)\%$
	Mass Density, $kg\ m^{-3}$		
950 km	$(1.27 \pm 0.15) \times 10^{-9}$	$(1.04 \pm 0.30) \times 10^{-9}$	$(6.21 \pm 1.23) \times 10^{-10}$
1050 km	$(2.73 \pm 0.22) \times 10^{-10}$	$(2.16 \pm 0.44) \times 10^{-10}$	$(1.40 \pm 0.22) \times 10^{-10}$
1200 km	$(3.18 \pm 0.08) \times 10^{-11}$	$(2.39 \pm 0.16) \times 10^{-11}$	$(1.74 \pm 0.18) \times 10^{-11}$
1400 km	$(2.35 \pm 0.09) \times 10^{-12}$	$(1.67 \pm 0.18) \times 10^{-12}$	$(1.40 \pm 0.05) \times 10^{-12}$

[a]For T_A and T_5, results from the fit of the combined ingress and egress data are presented, and the error bars correspond to horizontal variations between the ingress and egress results. The T_B error bars were estimated as twice those of T_A since only the egress data are available. These results do not take into account the systematic 20% instrumental error. The CH_4 mixing ratios at 1400 km were determined using a H_2 density of $\simeq 5 \times 10^5$ cm^{-3}.

recorded during T_5 (egress) and two times smaller than $(2.4 \pm 0.10) \times 10^6$ cm^{-3} recorded during T_A (ingress).

[16] The study of the atmospheric structure was performed when adequate data were available, i.e., for the data sets recorded during the ingress and egress portions of T_A and T_5 and the egress portion of T_B. The best fit profiles, obtained by using the diffusion model, were plotted as solid lines in Figure 4. These profiles also show a density extrapolation down to 900 km, providing an estimate of a 2.5% to 3.0% methane mixing ratio at 950 km. These values are slightly higher than the 2.4% methane mole fraction estimated by *Vervack et al.* [2004] from the Voyager ingress data, in the 950–1100 km altitude range, located just below the INMS measurements. It must be emphasized again that the present fits correspond to an isothermal atmosphere, with a constant eddy diffusion coefficient, assuming a negligible upward flux of methane.

[17] A periodic variation of the density about the best fit profiles reveal the presence of vertical and probably horizontal waves in Titan's upper atmosphere [*Waite et al.*, 2005b; *Yelle et al.*, 2006]. These waves, originating from complex dynamics, are described in more detail by *Müller-Wodarg et al.* [2006]. The wave pattern appeared to be stronger in the case of T_5 as compared to T_A and T_B. As a result, the best fits obtained for T_5 show more variations about the mean vertical profile.

[18] A combination of the INMS data and best fit results corresponding to four altitude levels are gathered in Table 2, displaying the N_2 and CH_4 density, the CH_4 mole fraction, and the atmospheric mass density. The atmospheric mass density was estimated by assuming that N_2 and CH_4 are the principal species. This assumption is justified at 1200 km and below since the density of H_2, the next most abundant species, was found to be an order of magnitude smaller than that of CH_4. The mass density estimated at 950 km after analysis of the T_A data, $(1.27 \pm 0.15) \times 10^{-9}$ $kg\ m^{-3}$, was found to be about 1.2 times larger than for T_B, $(1.04 \pm 0.30) \times 10^{-9}$ $kg\ m^{-3}$, and twice as large as for T_5, $(6.21 \pm 1.23) \times 10^{-10}$ $kg\ m^{-3}$.

[19] The temperature and eddy coefficient values obtained as a result of the nitrogen and methane simultaneous fit, assuming a negligibly small methane escape flux, are presented in Table 3 for T_A, T_B, and T_5. Owing to the calibration changes since the publication of the T_A atmospheric structure in the work of *Yelle et al.* [2006], the analysis was performed again on the T_A data. Slightly different numerical values were estimated but leave their conclusions unchanged. The temperatures were found to be 152.8 ± 4.6 K for T_A (compared to 149 ± 3 K in the work of *Yelle et al.* [2006]), 149.0 ± 9.2 K for T_B, and 157.4 ± 4.9 K for T_5. The error bars represent the horizontal variation traveled by the spacecraft during the flybys. (The T_B error bars are assumed to be twice those of T_A since the egress data only are available). Compared to T_A and T_B, the temperature corresponding to flyby T_5 was found to be 5 K and 8 K higher, respectively. Considering that T_5 occurred on the night side, whereas T_A and T_B occurred near the dusk terminator, these results are opposite to the effects expected from solar-driven mechanisms.

[20] It is also interesting to compare the temperature results found when fitting separately the ingress and egress data sets. In the case of T_A, the N_2 and CH_4 density data were well fit with 150.0 K for ingress and 157.4 K for egress. This 7.4 K temperature difference might be due to local time variations but can also be interpreted as the effect of vertical and/or horizontal waves in Titan's upper atmosphere [*Yelle et al.*, 2006]. In the case of T_5, a 8.2 K temperature variation was found between the ingress and egress data, but the opposite trend was observed. The ingress temperature (162.3 K) was found to be warmer than

Table 3. Atmospheric Structure Parameters of Titan's Upper Atmosphere, Obtained By Running the Diffusion Fitting Model on the T_A, T_B, and T_5 INMS Data Recorded Below 1500 km[a]

	T_A	T_B	T_5
	Temperature, K		
Combined data	152.8 ± 4.6	149.0 ± 9.2	157.4 ± 4.9
Ingress	150.0	Not enough data	162.3
Egress	157.4	149.0	154.1
	Eddy Diffusion Coefficient, $cm^2\ s^{-1}$		
Combined data	$(5.2^{+5.0}_{-2.9}) \times 10^9$	$(1.0^{+1.0}_{-0.58}) \times 10^{10}$	$(3.9^{+1.0}_{-0.9}) \times 10^9$
Ingress	2.3×10^9	Not enough data	3.0×10^9
Egress	1.2×10^{10}	1.0×10^{10}	4.9×10^9
Homopause altitude, km	1250 ± 60	1280 ± 120	1180 ± 30
Exobase altitude, km	1442 ± 7	1409 ± 14	1401 ± 2
Thickness of exobase layer, km	85 ± 2	81 ± 4	86 ± 3

[a]For T_A and T_5, the error bars correspond to horizontal variations between the ingress and egress results. The T_B error bars were estimated as twice those of T_A since the egress data only were available. The eddy coefficient values strongly depend on the assumption that no flux of CH_4 particles is traveling throughout Titan's upper atmosphere. The thickness of the exobase layer is determined as the value of the mean free path at the exobase.

the egress temperature (154.1 K). From these findings, it can be argued that the dusk region (egress T_A and ingress T_5) is warmer than both the afternoon region (ingress T_A) and night region (egress T_5). However, the differences with respect to Saturn's magnetospheric flow onto the exobase must also be explored. During T_A, the dusk terminator is located in the wake, whereas during T_5, the dusk terminator is located on the inward trailing hemisphere (Figure 1). Although additional data and modeling will be necessary, we note that the highest temperatures in both instances are on the Saturn facing hemispheres, where the pickup ion flux is expected to be largest.

[21] As shown in Table 3, the altitude of the exobase was estimated to be located between 1400 and 1450 km. These estimates were made by approximating the exobase as the altitude where the atmospheric scale height and the nitrogen mean free path are equal. In reality, the transition between the atmosphere and the exosphere is a wide altitude region, which cannot be adequately described by a precise altitude.

[22] The eddy diffusion coefficients were determined for each flyby as part of the four-parameter fit. The results were found to be $K = (5.2^{+5.0}_{-2.9}) \times 10^9\ cm^2\ s^{-1}$ for T_A, $K = (1.0^{+1.0}_{-0.58}) \times 10^{10}\ cm^2\ s^{-1}$ for T_B, and $K = (3.9^{+1.0}_{-0.9}) \times 10^9\ cm^2\ s^{-1}$ for T_5. With these values, estimates were made for the homopause altitude by setting the eddy diffusion coefficients equal to the binary molecular diffusion coefficients (D_{N2-CH4}). The homopause altitude was estimated to be 1250 ± 60 for T_A, 1280 ± 120 for T_B, and 1180 ± 30 for T_5 (Figure 5).

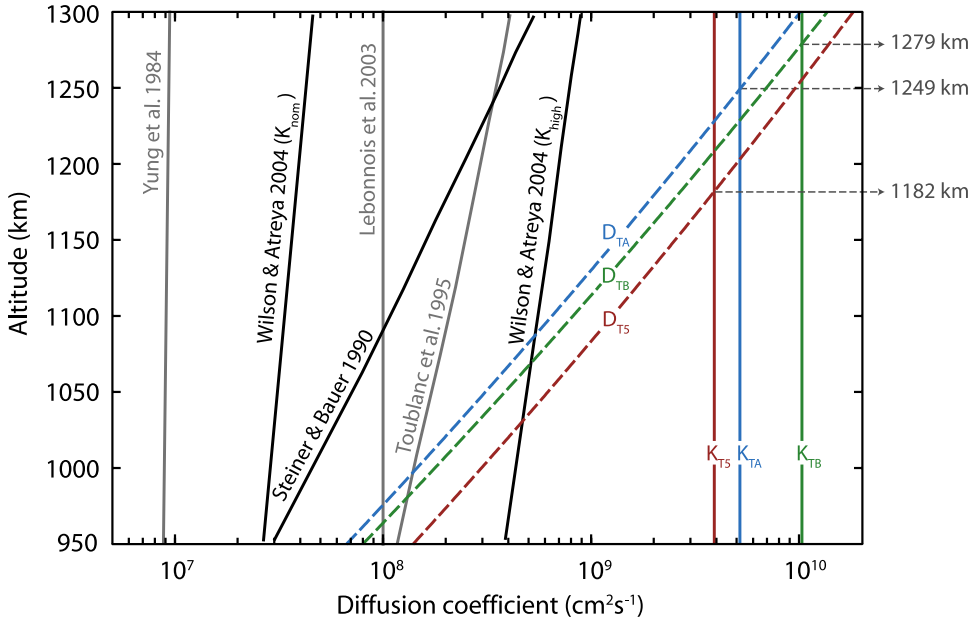

Figure 5. Eddy diffusion coefficients ($K_{TA,TB,T5}$) and homopause altitude levels, estimated from fitting the T_A, T_B, and T_5 INMS data. $D_{TA,TB,T5}$ represent the binary N_2-CH_4 coefficients for molecular diffusion. The eddy coefficient profiles obtained by *Steiner and Bauer* [1990] and used in the photochemical models of *Yung et al.* [1984], *Toublanc et al.* [1995], *Lebonnois et al.* [2003], and *Wilson and Atreya* [2004] are also plotted for comparison (black and grey solid lines).

Table 4. Exobase Temperature, T_c, Required to Fit the T_A, T_B, and T_5 INMS Data in the Exosphere[a]

		Thermal temperature, K z < 1500 km	T_c (N_2), K 1500 < z < 2000 km	T_c (CH_4), K 1500 < z < 2000 km
T_A	ingress	150.0	174	171
	egress	157.4	175	183
T_B	egress	149.0	203	215
T_5	ingress	162.3	149	149
	egress	154.1	205	223

[a]The fits were performed on data recorded between 1500 and 2000 km with a model of *Chamberlain* [1963], and are compared to the thermal temperature values, obtained from simultaneously fitting the N_2 and CH_4 INMS data between closest approach and 1500 km with a simple diffusion model.

[23] These large eddy coefficient values and high homopause altitudes are consistent with interpretations of the Voyager observations reported by *Strobel et al.* [1991] and *Vervack et al.* [2004]. They are also comparable to the calculations made by *Müller-Wodarg and Yelle*, 2002], who found a 10^9 cm^2 s^{-1} effective eddy diffusion coefficient as a consequence of vigorous dynamics in Titan's upper atmosphere. These eddy coefficient values are, however, much higher than that suggested by the study of *Steiner and Bauer* [1990], who applied a 1-D isothermal transport model for the minor gases in Titan's upper atmosphere, or those used in previous one-dimensional photochemical models, such as that of *Yung et al.* [1984], *Toublanc et al.* [1995], *Lebonnois et al.* [2003], and *Wilson and Atreya* [2004] (see Figure 5). As mentioned earlier, one should not rule out the possibility of the eddy coefficient being significantly smaller, if the methane escape flux is non-negligible. Although the methane escape flux cannot be due to Jeans escape (calculated to be negligible), the impact of a large number of energetic particles coming from Saturn's magnetosphere and penetrating into Titan's upper atmosphere can produce a population of suprathermal methane molecules, as can the production of hot methane molecules through ion-neutral chemistry.

3. Titan's Exosphere

[24] Here we focus on the data located above 1450 km, in Titan's exosphere. Thermal profiles were calculated for Titan's exospheric nitrogen and methane molecules, using the atmospheric temperatures derived in the previous section. In all cases except during the inbound leg of T_5, the N_2 and CH_4 density data were found to start diverging from these thermal profiles at altitudes above 1700 km, suggesting the presence of an enhanced suprathermal population. In an attempt to characterize the mechanism for producing that population, two exospheric models are constructed. First, using the method of *Chamberlain* [1963], the temperatures necessary to fit the exospheric N_2 and CH_4 density profiles, assuming a Maxwellian distribution at the exobase, are determined. A second model, using a different development of the Liouville theorem [*Schunk and Nagy*, 2000; *Kim*, 1991] is applied to determine the exobase energy distribution necessary to fit the N_2 and CH_4 data, as well as the associated suprathermal density, escape flux, and energy density.

3.1. Temperature at the Exobase

[25] A preliminary exospheric model is built using the method of *Chamberlain* [1963], which assumes a Maxwellian distribution at the exobase. This model is applied in attempting to fit the N_2 and CH_4 exospheric data. The parameters are T_c, the temperature at the exobase assumed to be constant throughout the exosphere, and n_c, the density of the species (N_2 or CH_4) at altitude z_c, the altitude of the exobase. These parameters are involved in the following system of equations:

$$\begin{aligned} n_s(z) &= \zeta[\lambda(z)] n_c e^{-(\lambda(z_c)-\lambda(z))}, \\ \lambda(z) &= \frac{G M_{Titan} m_s}{k_b T_c (R_{Titan}+z)}, \end{aligned} \tag{3}$$

where n_s and m_s are the density and mass of species s, G the gravitational constant, M_{Titan} and R_{Titan} the mass and the radius of Titan, k_b the Boltzmann constant, and ζ the partition function. The altitude z_c was assumed to be 1450 km, an altitude in good agreement with the results presented in Table 3. The exobase temperatures T_c obtained as a result of the exospheric fits, are listed in Table 4. Except for the ingress portion of T_5, these temperatures are found to be 20 to 70 K higher than the temperatures obtained using the diffusion model below 1500 km. The results of the exospheric fits as well as the thermal profiles are presented for T_A, T_B, and T_5 in Figure 6.

[26] These observations are attributed to the presence of a significant suprathermal population, deforming the velocity distribution by increasing its suprathermal tail at the exobase. In the following section, a different technique, based on the Liouville theorem, is used to estimate the corresponding energy distribution at the exobase, as well as the suprathermal density, energy deposition, and escape rate.

3.2. Energy Distribution at the Exobase

[27] A second exospheric model is constructed to characterize the suprathermal component, using the method developed by *Kim* [1991] and presented in equations (10.102)–(10.103) in the work of *Schunk and Nagy* [2000]. This model is based on the Liouville theorem and takes into account all particles that cross the exobase, i.e., particles traveling on ballistic and escaping trajectories. It involves the following system of equations for molecules with energy between $E - \Delta E/2$ and $E + \Delta E/2$:

$$\begin{aligned} \bar{v} \geq 1 : n(r,E,\Delta E) &= \left[\left(\bar{v}^2 - (1-y)\right)^{\frac{1}{2}} \right. \\ &\quad \left. - \left(\bar{v}^2(1-y^2) - (1-y)\right)^{\frac{1}{2}} \right] \frac{F_c}{2\bar{v}} \\ \frac{1}{(1+y)^{\frac{1}{2}}} \leq \bar{v} < 1 : & \\ n(r,E,\Delta E) &= \left[\left(\bar{v}^2 - (1-y)\right)^{\frac{1}{2}} - \left(\bar{v}^2(1-y^2)\right. \right. \\ &\quad \left. \left. - (1-y)\right)^{\frac{1}{2}} \right] \frac{F_c}{\bar{v}} \\ (1-y)^{\frac{1}{2}} \leq \bar{v} < \frac{1}{(1+y)^{\frac{1}{2}}} : & \\ n(r,E,\Delta E) &= \left(\bar{v}^2 - (1-y)\right)^{\frac{1}{2}} \frac{F_c}{\bar{v}}, \end{aligned} \tag{4}$$

where $y = r_c/r$ is the ratio between the radial distance at the exobase and a point in the exosphere, $\bar{v} = \frac{v_c}{v_{esc}}$ is the ratio of

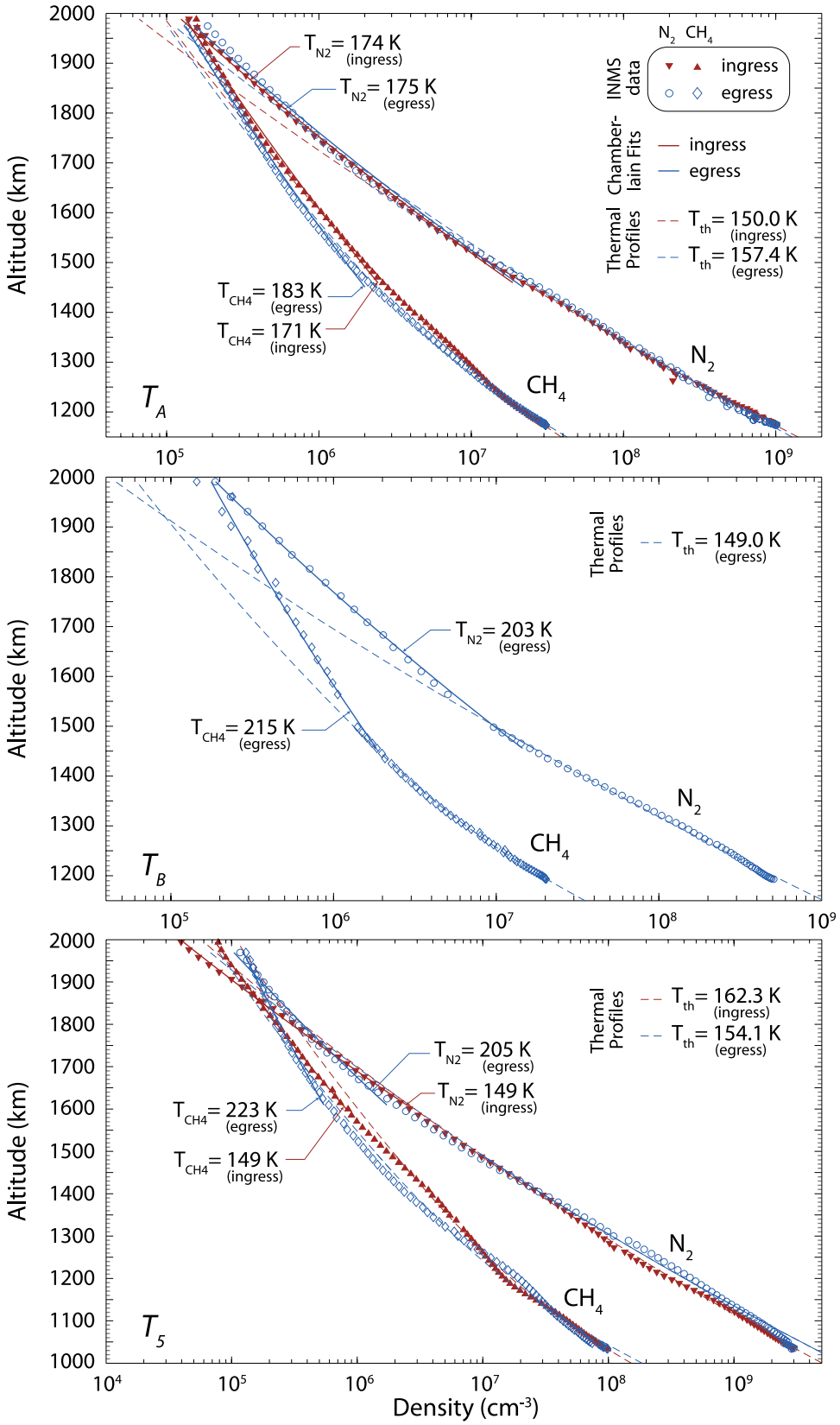

Figure 6. Results of the fit of the N_2 and CH_4 density data recorded by INMS in Titan's exosphere during flybys T_A, T_B, and T_5, using the method of *Chamberlain* [1963]. The thermal profiles are represented with dash lines and the fit profiles with solid lines (red for ingress and blue for egress). The corresponding temperatures are indicated in the legends and on the graphs.

the particle's velocity at the exobase over the escape velocity, $v_{esc} = \sqrt{\frac{2GM}{r_c}}$, and F_c is the number density of particles at the exobase with energy between $E - \Delta E/2$ and $E + \Delta E/2$. Here again, the exobase altitude was chosen to be at 1450 km.

[28] Various shapes were tested for the energy distribution at the exobase, ($f_c = \frac{F_c}{\Delta E}$): an analytical power function, f_c^A, a two-parameter power function, f_c^B, an added Maxwellian-like function, f_c^C, and a kappa function, f_c^κ. The analytical power function was chosen to reproduce the energy spectrum presented by *Johnson* [1990, 1994] for the cascade of collisions initiated by incident heavy ions. In these studies, the linear sputtering problem was examined, assuming a flat atmosphere and dividing the particles into two classes: the fast particles with speeds much greater than $\bar{v}$, and the thermal particles. Following equations (6) to (10) in the work of *Johnson* [1994], the analytical power function was defined using the Maxwellian distribution when $E \leq 4kT_c$, the chosen threshold, to which was added the energy distribution of the cascade particles when $E > 4kT_c$:

$$\begin{aligned} E \leq 4kT_c \ &\rightarrow f_c^A(E) = f_c^M(E), \\ E > 4kT_c &\rightarrow f_c^A(E) = f_c^M(E) + n_c \frac{A}{(E/kT_c)^{\frac{5}{2}}} \frac{1}{kT_c}, \end{aligned} \tag{5}$$

where A is the free-parameter used for the data fit, n_c is the total density at the exobase, T_c the atmospheric temperature at the exobase, and $f_c^M(E)$ the Maxwellian distribution expressed as:

$$f_c^M(E) = n_c \frac{2}{\sqrt{\pi}} \sqrt{\frac{E}{kT_c}} e^{-\frac{E}{kT_c}} \frac{1}{kT_c}. \tag{6}$$

[29] The *two-parameter power function* was defined in the same way as the analytical power function, but with a suprathermal tail characterized by two free parameters, A and x, such that:

$$E > 4kT_c \rightarrow f_c^B(E) = f_c^M(E) + n_c \frac{A}{(E/kT_c)^x} \frac{1}{kT_c}. \tag{7}$$

[30] Although the two-parameter power function allows a less constrained fit of the INMS data, the best fit parameter, x, directly controls the stiffness of the high energy leg of the distribution. In particular, the escape flux and energy density integrals will not converge if $x \leq \frac{3}{2}$ and if $x \leq \frac{5}{2}$, respectively, and parameters derived heavily depend on a choice of a high-energy cutoff. However, because the analytical power function is based on a physical model, the energy density deposited at the exobase and the escape flux can be estimated.

[31] Taking these considerations into account, two additional models for the exobase energy spectrum were tested with slopes steep enough on both sides of the distribution to avoid threshold or cutoff dependency. First, the added Maxwellian-like function was chosen in an attempt to describe the presence of two populations with different average temperatures. This distribution is determined as the sum of the Maxwellian distribution characterized by parameters n_c and T_c, and a Maxwellian-like distribution characterized by two free parameters, n_1 and T_1:

$$f_c^C(E) = f_c^M(E) + n_1 \frac{2}{\sqrt{\pi}} \sqrt{\frac{E}{kT_1}} e^{-\frac{E}{kT_1}} \frac{1}{kT_1}. \tag{8}$$

[32] Second, a kappa function, which is essentially a sum of Maxwellians, was tested with the goal of modeling the thermal and the hot particles in a single distribution. The kappa function, often used to fit plasma energy spectra, can also describe neutral distributions that are not fully thermalized [e.g., *Jurac et al.*, 2002]. It is expressed as a two-parameter function after normalization:

$$f_c^\kappa(E) = \frac{n_c}{\frac{\sqrt{\pi\kappa}}{2}\gamma\left(\kappa - \frac{1}{2}\right)\gamma(\kappa)} \frac{1}{\left(1 + \frac{E}{\kappa kT_0}\right)^{\kappa+1}} \sqrt{\frac{E}{kT_0}} \frac{1}{kT_0}, \tag{9}$$

where κ and T_0 are the fit parameters, and $\gamma(x) = \int_0^\infty t^{x-1} e^{-t} dt$ is the gamma function.

[33] The best fits of the N_2 and CH_4 INMS exospheric data were obtained using the kappa function. The corresponding exospheric density profiles are presented for T_A, T_B, and T_5 in Figure 7. Despite the lower quality of the fit, we also present the analytical power function, which is based on a physical model for the coronal heating and escape. The best fit-parameters are listed in Tables 5 and 6 for the analytical power function and kappa function, respectively. The corresponding energy distribution shapes are plotted in Figure 8. Knowing the energy distributions, estimates were also made at the exobase for the density of the suprathermal population, n^*, and the escape flux, Φ_{esc}, using the following expressions:

$$n^* = \int_{E > \frac{kT}{2}} \left(f_c(E) - f_c^M(E)\right) dE, \tag{10}$$

$$\Phi_{esc} = \frac{1}{4} \int_{E > E_{esc}} f_c(E) \sqrt{\frac{2E}{m}} dE, \tag{11}$$

where m is the molecular mass of the particle and $E_{esc} = \frac{GMm}{r_c}$ is the escape energy. The condition $E > \frac{kT}{2}$ was added in equation (10) to discard the low-energy portion of the kappa function with density larger than the Maxwellian. An estimate of the energy density per unit time deposited in the production of the suprathermal particles in the exobase layer was also estimated from both fits. It was calculated numerically for the kappa function:

$$E_D^* = \frac{1}{4\lambda} \int_{E > \frac{kT}{2}} \left(f_c^\kappa(E) - f_c^M(E)\right) \sqrt{\frac{2E}{m}} E dE, \tag{12}$$

where λ represents the thickness of the exobase layer approximated as 85 km, a value in good agreement with the results presented in Table 3. Also, it was determined analytically for the analytical power function, using the

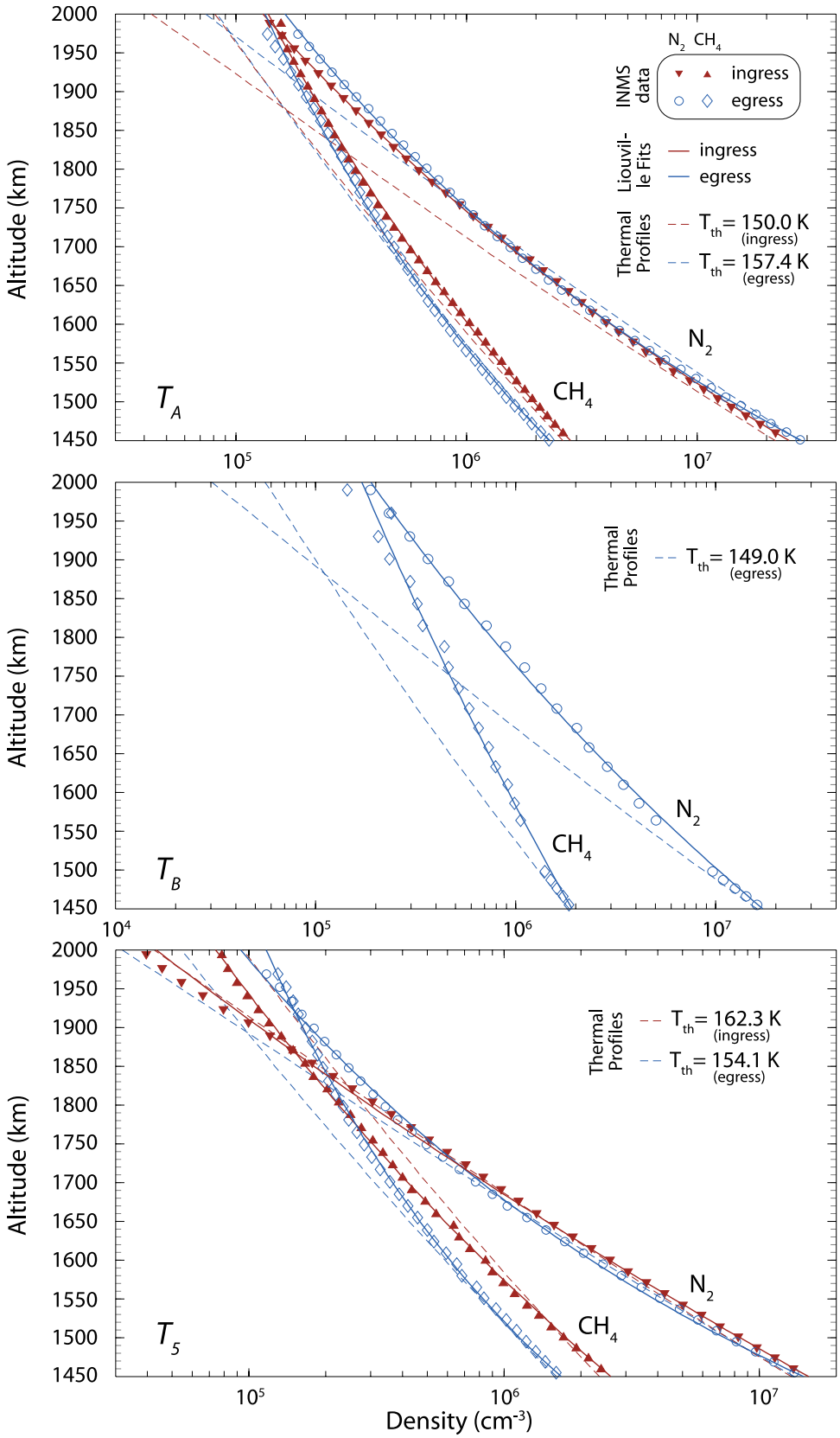

Figure 7. Results of the fit of the N_2 and CH_4 density data recorded by INMS in Titan's exosphere during flybys T_A, T_B, and T_5, using the method presented by *Schunk and Nagy* [2000] based on the Liouville theorem. The thermal profiles are represented with dash lines and the fit profiles with solid lines (red for ingress and blue for egress).

Table 5. Parameters of the Analytical Energy Distribution Resulting From the Fit of the INMS T_A, T_B, and T_5 Exospheric Data Using the Model Presented By *Schunk and Nagy* [2000] Based on the Liouville Theorem[a]

			Atmospheric Parameters		Result Fit Parameters		Parameters Characterizing Suprathermal Populations		
			T_c, K	n_c, cm^{-3}	A	χ^2	n^*, cm^{-3}	Φ_{esc}, cm^{-2} s^{-1}	E_D^*, eV cm^{-3}s^{-1}
N_2	T_A	ingress	150.0	2.50×10^7	1.3×10^{-1}	9×10^{-4}	4.4×10^5	4.9×10^8	1.5×10^2
		egress	157.4	2.83×10^7	8.1×10^{-2}	3×10^{-3}	3.1×10^5	3.7×10^8	1.1×10^2
	T_B	egress	149.0	1.72×10^7	4.9×10^{-1}	2×10^{-2}	1.2×10^6	1.3×10^9	3.8×10^2
	T_5	ingress	162.3	1.56×10^7	-3.0×10^{-3}	1×10^{-2}	NA	NA	NA
		egress	154.1	1.49×10^7	1.2×10^{-1}	1×10^{-2}	2.5×10^5	2.8×10^8	8.6×10^1
CH_4	T_A	ingress	150.0	2.82×10^6	2.5×10^{-1}	3×10^{-3}	9.4×10^4	2.4×10^8	4.2×10^1
		egress	157.4	2.29×10^6	2.6×10^{-1}	2×10^{-3}	8.1×10^4	2.2×10^8	3.8×10^1
	T_B	egress	149.0	1.92×10^6	1.1	1×10^{-2}	2.9×10^5	7.3×10^8	1.3×10^2
	T_5	ingress	162.3	2.62×10^6	-3.0×10^{-3}	1×10^{-2}	NA	NA	NA
		egress	154.1	1.67×10^6	4.3×10^{-1}	9×10^{-3}	9.9×10^4	2.6×10^8	4.5×10^1

[a]Here T_c is the isothermal temperature determined by fitting the INMS data below 1500 km; n_c is the density at the exobase assumed to be located at 1450 km; A is the fit parameter characterizing the energy distribution of the suprathermal tail at the exobase; χ^2 is the parameter characterizing the quality of the fit; n^* is the density of the suprathermal particles at the exobase; Φ_{esc} is the escape flux at the exobase; E_D^* is the energy deposition rate in the exobase layer. (A deposited energy flux can be inferred from multiplying E_D^* by the thickness of the exobase layer, λ = 85 km.)

following expression derived from equation (10) in the work of *Johnson* [1994]:

$$E_D^* = \frac{1}{\lambda}\frac{An_c}{\beta}\sqrt{\frac{2}{m}}(kT_c)^{\frac{3}{2}}, \quad (13)$$

where A is the fit-parameter for the analytical model and β is a parameter that depends on interaction potential, approximated as $\simeq$1 for the hard sphere collision assumption. The suprathermal density, escape flux, and energy density results are also presented in Tables 5 and 6.

3.3. Results and Discussion

[34] For all configurations, except T_5-ingress, the best fits of the nitrogen and methane INMS exospheric data show energy distributions with a suprathermal component, implying a significant source of suprathermal molecules at the exobase (Figure 8). Among all tested distribution shapes, the kappa function was found to have the steepest suprathermal tail, whereas the analytical model had the flattest tail. These two distributions therefore provide rough lower and upper bounds, respectively, for the escape flux and energy deposition rate. This trend, however, does not apply to the estimates of the suprathermal density, which depends strongly on the number of close-to-thermal particles. For example in the case of T_B, although the escape flux and energy density are found to be greater using the analytical power function versus the kappa function, the estimated suprathermal density above the nominal cut-off is smaller.

[35] The results of the present study suggest densities of hot N_2 molecules ranging between 1.1×10^5 cm^{-3} and 1.6×10^6 cm^{-3}, and densities of hot CH_4 molecules ranging between 7.0×10^4 cm^{-3} and 3.1×10^5 cm^{-3} (Tables 5 and 6). *Michael and Johnson* [2005] showed in their 1-D DSMC study of local sputtering that the ion flux produced an enhanced temperature of $\simeq$7 K and an enhanced density of $\simeq$30% at 1600 km (see their Figure 3). This density enhancement is smaller than the 40% enhancement observed in the T_B N_2 data at 1600 km but is larger than the enhancements for T_A and T_5, which start above 1700 km. In fact, in the T_A and T_5 egress configurations, the modeled N_2 thermal density at 1600 km appears greater than the local data points, due to the presence of waves in Titan's upper atmosphere. The density enhancement at this altitude may not therefore constitute a viable basis for comparison between data and model. In the present study, the slope of the enhanced N_2 density profile between 1800 km and 2000 km was found to be between 23% and 32% flatter than the slope of the thermal profile, whereas *Michael and Johnson* [2005] find a smaller decrease in the slope, between 1425 km and 1600 km, roughly 12% consistent with a much lower-energy deposition rate as described below.

Table 6. Parameters of the Kappa Energy Distribution Resulting From the Fit of the INMS T_A, T_B, and T_5 Exospheric Data Using the Model Presented By *Schunk and Nagy* [2000] Based on the Liouville Theorem[a]

			Result Fit Parameters			Parameters Characterizing Suprathermal Populations		
			κ	T_0, K	χ^2	n^*, cm^{-3}	Φ_{esc}, cm^{-2} s^{-1}	E_D^*, eV cm^{-3}s^{-1}
N_2	T_A	ingress	14.8	138.0	5×10^{-4}	3.0×10^5	1.4×10^3	6.1×10^1
		egress	8.86	119.9	4×10^{-4}	1.4×10^5	1.3×10^5	4.7×10^1
	T_B	egress	18.7	172.3	3×10^{-3}	1.6×10^6	1.2×10^3	2.0×10^2
	T_5	ingress	85.7	147.9	4×10^{-3}	6.4×10^{-1}	2.8×10^{-5}	7.0×10^{-4}
		egress	7.78	115.5	2×10^{-3}	1.1×10^5	2.2×10^5	3.4×10^1
CH_4	T_A	ingress	8.74	134.2	5×10^{-4}	7.7×10^4	1.5×10^6	2.1×10^1
		egress	5.85	126.7	6×10^{-4}	7.0×10^4	1.3×10^7	2.6×10^1
	T_B	egress	97.8	210.5	5×10^{-3}	3.1×10^5	4.9×10^3	4.9×10^1
	T_5	ingress	17.0	126.4	5×10^{-4}	4.0×10^2	7.5×10^3	2.7×10^{-1}
		egress	4.26	118.8	5×10^{-4}	8.6×10^4	5.1×10^7	3.6×10^1

[a]Here κ, T_0 are the fit parameters characterizing the energy distribution at the exobase; χ^2 is the parameter characterizing the quality of the fit; n^* is the density of the suprathermal particles at the exobase; Φ_{esc} is the escape flux at the exobase; E_D^* is the energy deposition rate in the exobase layer. (A deposited energy flux can be inferred from multiplying E_D^* by the thickness of the exobase layer, λ = 85 km.)

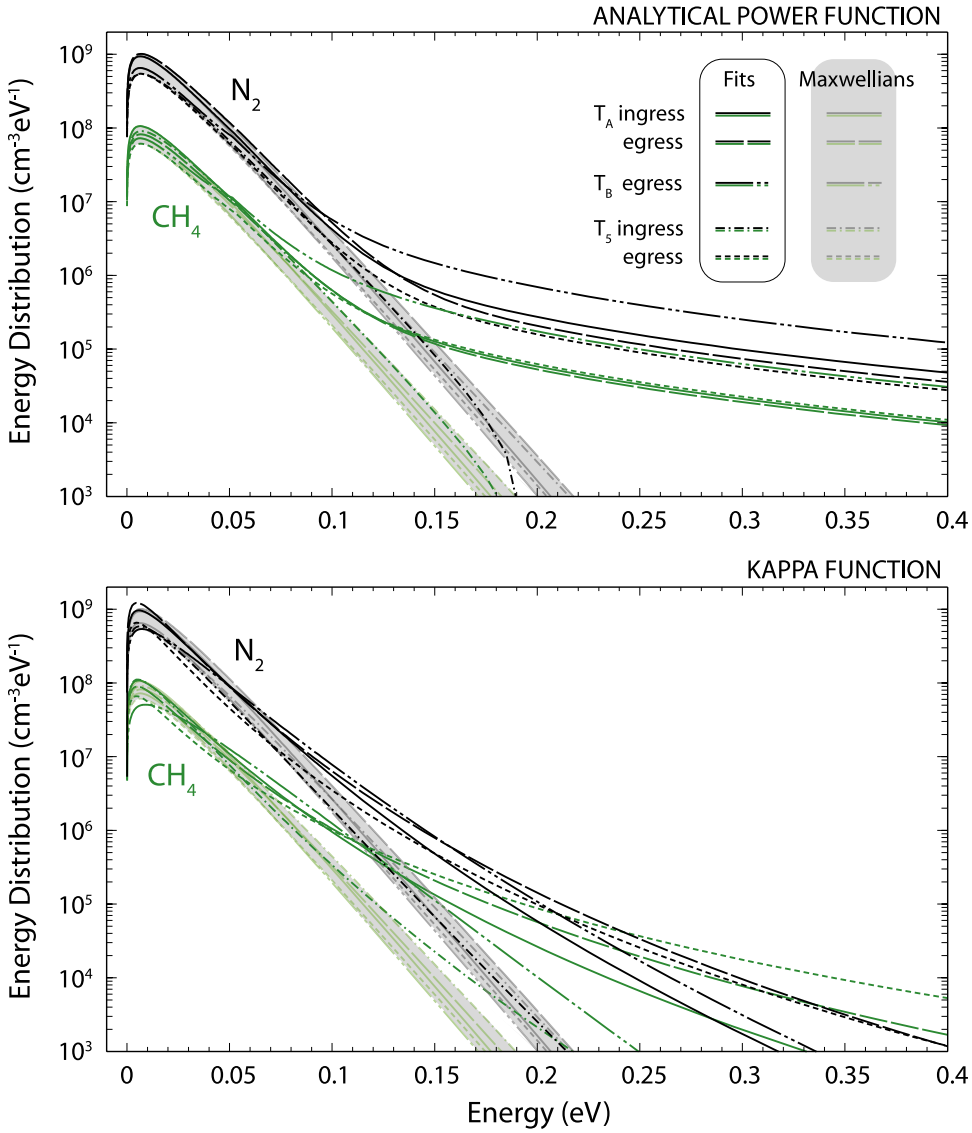

Figure 8. Energy distribution at the exobase for N_2 and CH_4 obtained from the fit of the INMS T_A, T_B, and T_5 exospheric data, using the method presented by *Schunk and Nagy* [2000] based on the Liouville theorem. Results are presented for the two following energy distribution shapes: (top) analytical power law and (bottom) kappa function.

[36] From the data analyses of the inbound and outbound legs of T_A and of the outbound leg of T_5, the energy deposition rate in the exobase layer was estimated to range between $4.7 \pm 1.0 \times 10^1$ eV cm^{-3} s^{-1} (kappa function) and $1.2 \pm 0.3 \times 10^2$ eV cm^{-3} s^{-1} (analytical power function) for N_2 and between $2.8 \pm 0.7 \times 10^1$ eV cm^{-3} s^{-1} (kappa function) and $4.2 \pm 0.3 \times 10^1$ eV cm^{-3} s^{-1} (analytical power function) for CH_4. These values represent about 20 to 40% of the maximum energy deposited by solar EUV radiation ($\simeq 4 \times 10^2$ eV cm^{-3} s^{-1} at 1000 km as estimated by *Michael and Johnson* [2005]). Larger values for the energy density and energy flux were found for the outbound leg of T_B, but these data have larger uncertainties due to a lower signal value, which occurs at a >60° angle of attack.

[37] In the work of *Michael and Johnson* [2005], the energy deposited into the atmospheric nitrogen molecules by the slowed and deflected N^+ magnetospheric ions and by the molecular pickup ions was calculated and shown to dominate the UV flux absorbed in the exobase region. Using the 1-D DSMC method with and exobase at 1500 km, they obtained an energy deposition <10^1 eV cm^{-3} s^{-1} by the N^+ ions (with a peak of 6.5×10^1 eV cm^{-3} s^{-1} at $\simeq$1150 km), and an energy deposition of $\simeq 2.5 \times 10^1$ eV cm^{-3} s^{-1} by the molecular pick-up ions (with a peak of $\simeq 1.2 \times 10^2$ eV cm^{-3} s^{-1} at $\simeq$1130 km). These rates, which are global averages based on the plasma ion fluxes from *Brecht et al.* [2000], are about two to five times smaller than the energy density inferred from the T_A ingress and egress and the T_5 egress data. Therefore it is clear that in some passes the exobase is heated by a process that deposits much more energy in the exobase region than UV heating or the global average flux used by *Michael and Johnson* [2005]. Earlier, *Lammer et al.* [1998] and *Shematovich et al.* [2001] used an energy deposition rate in which only the ambient N^+ were assumed to penetrate the atmosphere. This gives an even smaller energy deposition rate close to the exobase.

[38] The neutral N_2 or CH_4 data recorded by INMS below 2000 km mainly consist of molecules in ballistic orbits, whose density masks that of the molecules in escaping orbits. In fact, to be able to measure directly the populations of escaping N_2 and CH_4 molecules, neutral density data would need to be recorded at very large distances from Titan, i.e., in regions where the density is far below INMS' range of sensitivity. Therefore the constraints on the escape flux are much poorer than they are on the energy deposition rates, and although the quality of the fits was found to be twice as good with the kappa function as with the analytical power function, the lower bounds do not constrain the escape flux very well except, possibly, for the CH_4 flux at T_A and T_5. Using incrementally decreasing cutoffs for the analytical and kappa energy distributions, the energy of the particles detected by INMS in the exosphere below 2000 km was estimated to be lower than $\simeq$1 eV for N_2 and lower than $\simeq$0.3 – 0.5 eV for CH_4.

[39] *Michael et al.* [2005] calculated a globally averaged loss of nitrogen as either N or N_2 of $\simeq 3.7 \times 10^{25}$ N s^{-1}, corresponding to an average escape flux of $\simeq 1.8 \times 10^7$ N cm^{-2} s^{-1} assuming an exobase area of $\simeq 2.1 \times 10^{18}$ cm^2. These are much lower than the rough upper bounds in Table 5 obtained from the analytic model for most of the exobase crossings, except T_5 which, in the absence of data at higher altitudes, is consistent with no escape. The rough upper bounds to the CH_4 escape flux obtained from the analytic model for T_A are about one fourth the upper limit to the CH_4 escape flux estimated by *Yelle et al.* [2006] ($\simeq 1 \times 10^9$ CH_4 cm^{-2} s^{-1} referred to the exobase altitude) when they used a very low value for the eddy diffusion coefficient.

[40] Because the simple analytic model does not include energy dissipation by collisional dissociation, we use the energy deposition rates to obtain a better estimate the escape flux. Within the linear cascade model [*Johnson*, 1994] and assuming pickup ions are the dominant sputtering agent, we multiply the average energy deposition rates by the ratio of the escape rate in the work of *Michael et al.* [2005] to the energy deposition rate in the work of *Michael and Johnson* [2005]. For an average energy deposition rate of $\simeq$25 eV cm^{-3} s^{-1} at their exobase altitude, 1500 km, they obtain a nitrogen atom escape flux, as either N or N_2, of $\simeq 1.8 \times 10^7$ N cm^{-2} s^{-1}. Using the average of the energy deposition rates obtained from the kappa and the analytic model, and noting the CH_4 mass is comparable to that of N, very rough escape fluxes of 7.6, 5.7, 20.9, 0.0, 4.3×10^7 N cm^{-2} s^{-1} and $2.3, 2.3, 6.4, 0.0, 2.9 \times 10^7$ CH_4 cm^{-2} s^{-1} are implied for T_A ingress and egress, T_B egress, and T_5 ingress and egress, respectively. With the exception of T_5 ingress, the nitrogen escape rates are larger than the average escape flux in the work of *Michael et al.* [2005], but the CH_4 escape fluxes are more than an order of magnitude smaller than the upper bound for T_A from *Yelle et al.* [2006].

[41] The results in Tables 5 and 6 show the absence of a detectable suprathermal tail in the T_5 ingress INMS data. As discussed above, the density profiles and hence the derived temperature are affected by gravity waves [*Yelle et al.*, 2006; *Müller-Wodarg et al.*, 2006] and by plasma-induced heating [*Michael and Johnson*, 2005]. Therefore the higher temperature on T_5 ingress could mask the hot corona component below 2000 km. In any case, the analysis above indicates that the presence of a spatially variable population of suprathermal particles in Titan's exosphere involves local as opposed to globally averaged energy deposition mechanisms. The fact that significant densities of suprathermal N_2 and CH_4 are observed during egress but not ingress could also be interpreted as a contamination of the INMS closed source (particles remaining in the instrument) after passage of INMS through Titan's atmosphere. However, the contamination interpretation would be flyby-dependent since the suprathermal effects were observed both during the ingress and the egress portions of T_A.

4. Conclusions

[42] The study of the INMS N_2 and CH_4 density data, recorded during flybys T_A, T_B, T_5, and T_7, emphasizes the complexity of the dynamical mechanisms taking place in Titan's upper atmosphere. Large local time and latitudinal variations were observed between flybys and portions of flybys in the density profiles. At 1470 km, the total density recorded by INMS was found to be more than twice as large during T_A (at a latitude of 42°N) as during T_5 (52°N) or T_7 (52°S), indicating unexplained variation in density. The atmospheric structure parameters were determined by simultaneously fitting the N_2 and CH_4 density data using a diffusion model. The best fits were obtained using isothermal profiles with values 152.8 ± 4.6 K for T_A, 149.0 ± 9.2 K for T_B, and 157.4 ± 4.9 K for T_5, which suggests a temperature of about 5 K warmer at night than at dusk, a trend opposite to that predicted by solar-driven models. Therefore we suggest that spatial and temporal variations in the plasma flux are responsible for the variations in temperature and the variations in the hot corona densities discussed below.

[43] The study of the exospheric T_A, T_B, and T_5 observations showed the presence of significant N_2 and CH_4 suprathermal populations, with averaged density $4.4 \pm 5.1 \times 10^5$ cm^{-3} for hot N_2 and $1.1 \pm 0.9 \times 10^5$ cm^{-3} for hot CH_4 but no suprathermal component for ingress-T_5. The averaged energy deposition rates required to produce the observed hot corona were found to be $1.1 \pm 0.9 \times 10^2$ eV cm^{-3} s^{-1} and $3.9 \pm 3.5 \times 10^1$ eV cm^{-3} s^{-1} for N_2 and CH_4, respectively, but again were negligible for T_5 ingress. In order to characterize the mechanisms responsible for the INMS exospheric observations, further investigations are required. In addition to energy deposition by the UV and energy transport by gravity waves and thermospheric flow, the complex interaction between Titan's upper atmosphere and Saturn's magnetosphere needs to be described. Of particular interest is the puzzling observation of a high thermospheric temperature but the lack of a hot corona on the ingress portion of T_5. This pass occurred at high latitudes, on the magnetospheric ram and nightside.

[44] Pickup ion induced heating, which is the dominant atmospheric sputtering agent, appears to be a likely candidate for producing the hot components of Titan's corona. Assuming that incident pickup ions are the dominant atmospheric sputtering mechanism, as in the work of *Michael et al.* [2005], we use the average of the energy deposition rates obtained from the kappa and the analytic fits to estimate escape rates: $\simeq 7.7 \times 10^7$ N cm^{-2} s^{-1} and 2.8×10^7 CH_4 cm^{-2} s^{-1}.

[45] The latter is more than an order of magnitude smaller than the upper limit discussed by *Yelle et al.* [2006] for T_A, and therefore would be consistent with the large eddy diffusion coefficients derived here $\simeq$(4 to 10) $\times$ 10^9 cm^2 s^{-1}. On the basis of this average atmospheric loss rate, Titan would lose its present methane content in $\simeq$2.3 Gyr. The rough upper limit from the analytic model, averaged over the four cases, is $\simeq 3.6 \times 10^8$ CH_4 cm^{-2} s^{-1}, which is also consistent with a large eddy diffusion coefficient but would imply that the present methane inventory would be lost in $\simeq$0.2 Gyr. However, both of these are much longer than the photochemical lifetime of methane [*Wilson and Atreya*, 2004] so that atmospheric methane is recycled or supplied much faster than it is lost to space.

[46] The average nitrogen loss rate given above is about 5 times larger than the average in the work of *Michael et al.* [2005] and is consistent with losing $\simeq$5% of the present nitrogen inventory in 4 Gyr [*Johnson*, 2004]. This becomes $\simeq$75% using the averaged rough upper bound from the analytic fit ($\simeq 1.22 \times 10^9$ N cm^{-2} s^{-1}). Therefore the process that produces the hot corona might induce considerable atmospheric loss over Titan's lifetime.

[47] On the basis of the INMS observation and the analysis here, the loss rates above are likely to differ considerably depending on the latitude and longitude of the exobase crossing and the orientation of the solar illumination to the plasma flow. Hybrid models [*Brecht et al.*, 2000] indicate that the pickup ion flux varies across the exobase, with the dominant ion flux onto the trailing sunward quadrant but the dominant energy flux onto the trailing Saturn-facing quadrant. In addition, such models show that this flux varies with the solar illumination [*Kallio et al.*, 2004]. Therefore the pickup ion induced heating would be expected to be asymmetric across the exobase and depend on the local time. The five exobase crossings described all involve different geometries or local times. Therefore data from additional passes will need to be analyzed to obtain a model for the effect of the pickup ions on Titan's thermosphere. In addition, more accurate Monte Carlo simulations are needed to describe the effects of the incident ions. Such simulations need to include repeated charge exchanges between energetic magnetospheric ions or pickup ions and atmospheric neutrals, traveling along the penetrating magnetospheric fields into Titan's upper atmosphere, as well as pickup below the exobase.

[48] Finally, as suggested by *Cravens et al.* [1997], the complex photochemistry that takes place in Titan's upper atmosphere constitutes a nonnegligible source of hot neutrals in Titan's corona. This matter, and in particular the number and energy distribution of suprathermal particles produced by exothermic ion and neutral chemistry, is examined in detail within the context of the INMS observations by *De La Haye et al.* [2007].

[49] **Acknowledgments.** This research was supported by the NASA Jet Propulsion Laboratory contract 1283095, NASA task order NMO710023, Support INMS Instrument on Cassini Spacecraft During Tour.

[50] Wolfgang Baumjohann thanks the reviewers for their assistance in evaluating this paper.

References

Brecht, S. H., J. G. Luhmann, and D. J. Larson (2000), Simulation of the Saturnian magnetospheric interaction with Titan, *J. Geophys. Res.*, *105*, 13,119–13,130.

Chamberlain, J. W. (1963), Planetary coronae and atmospheric evaporation, *Planet. Space Sci.*, *11*, 901–960.

Cravens, T. E., C. N. Keller, and B. Ray (1997), Photochemical sources of non-thermal neutrals for the exosphere of Titan, *Planet. Space Sci.*, *45*, 889–896.

Cravens, T. E., et al. (2006), The composition of Titan's ionosphere, *Geophys. Res. Lett.*, *33*, L07105, doi:10.1029/2005GL025575.

De La Haye, V., J. H. Waite Jr., T. E. Cravens, A. F. Nagy, R. V. Yelle, R. E. Johnson, S. Lebonnois, and I. P. Robertson (2007), Titan's corona: The contribution of exothermic chemistry, *Icarus*, doi:10.1016/j.icarus.2007.04.031, in press.

Gan, L., C. N. Keller, and T. E. Cravens (1992), Electrons in the ionosphere of Titan, *J. Geophys. Res.*, *97*, 12,136–12,151.

Johnson, R. E. (1990), *Energetic Charged Particle Interactions with Atmospheres and Surfaces*, Springer, New York.

Johnson, R. E. (1994), Plasma-induced sputtering of an atmosphere, *Space Sci. Rev.*, *69*, 215–253.

Johnson, R. E. (2004), Magnetospheric plasma-driven evolution of satellite atmospheres, *Astrophys. J.*, *609*, L99–L102.

Jurac, S., M. A. McGrath, R. E. Johnson, J. D. Richardson, V. M. Vasyliunas, and A. Eviatar (2002), Saturn: Search for a missing water source, *Geophys. Res. Lett.*, *29*(24), 2172, doi:10.1029/2002GL015855.

Kallio, E., I. Sillanpää, and P. Janhunen (2004), Titan in subsonic and supersonic flow, *Geophys. Res. Lett.*, *31*, L15703, doi:10.1029/2004GL020344.

Keller, C. N., T. E. Cravens, and L. Gan (1992), A model of the ionosphere of Titan, *J. Geophys. Res.*, *97*, 12,117–12,135.

Kim, J. (1991), Model studies of the ionosphere of Venus: Ion composition, energetics and dynamics, Ph.D. thesis, Univ. of Mich., Ann Arbor.

Lammer, H., and S. J. Bauer (1991), Nonthermal atmospheric escape from Mars and Titan, *J. Geophys. Res.*, *96*, 1819–1825.

Lammer, H., and S. J. Bauer (1993), Atmospheric mass loss from Titan by sputtering, *Planet. Space Sci.*, *41*, 657–663.

Lammer, H., W. Stumptner, and S. J. Bauer (1998), Dynamic escape of H from Titan as consequence of sputtering induced heating, *Planet. Space Sci.*, *46*, 1207–1213.

Lebonnois, S., E. L. O. Baskes, and C. P. McKay (2003), Atomic and molecular hydrogen budget in Titan's atmosphere, *Icarus*, *161*, 474–485.

Michael, M., and R. E. Johnson (2005), Energy deposition of pickup ions and heating of Titan's atmosphere, *Planet. Space Sci.*, *53*, 263–267.

Michael, M., R. E. Johnson, F. Leblanc, M. Liu, J. G. Luhmann, and V. I. Shematovich (2005), Ejection of nitrogen from Titan's atmosphere by magnetospheric ions and pick-up ions, *Icarus*, *175*, 263–267.

Müller-Wodarg, I. C. F., and R. V. Yelle (2002), The effect of dynamics on the composition of Titan's upper atmosphere, *Geophys. Res. Lett.*, *29*(23), 2139, doi:10.1029/2002GL016100.

Müller-Wodarg, I. C. F., R. V. Yelle, N. Borggren, and J. H. Waite Jr. (2006), Waves and horizontal structures in Titan's thermosphere, *J. Geophys. Res.*, *111*, A12315, doi:10.1029/2006JA011961.

Press, W. H., S. A. Teukolsky, W. T. Vetterling, and B. P. Flannery (1996), *Numerical Recipes in Fortran 77: The Art of Scientific Computing*, 2nd ed., Cambridge Univ. Press, New York.

Schunk, R. W., and A. F. Nagy (2000), *Ionospheres: Physics, Plasma Physics, and Chemistry*, Cambridge Univ. Press, New York.

Shematovich, V. I. (1998), Kinetic modeling of suprathermal nitrogen atoms in the Titan's atmosphere. I. Sources, *Sol. Syst. Res.*, *32*, 384–391.

Shematovich, V. I., C. Tully, and R. E. Johnson (2001), Suprathermal nitrogen atoms and molecules in Titan's corona, *Adv. Space Res.*, *27*, 1875–1880.

Shematovich, V. I., R. E. Johnson, M. Michael, and J. G. Luhmann (2003), Nitrogen loss from Titan, *J. Geophys. Res.*, *108*(E8), 5087, doi:10.1029/2003JE002094.

Smith, G. R., D. F. Strobel, A. L. Broadfoot, B. R. Sandel, D. E. Shemansky, and J. B. Holberg (1982), Titan's upper atmosphere: Composition and temperature form the EUV solar occultation results, *J. Geophys. Res.*, *87*, 1351–1359.

Steiner, G., and S. J. Bauer (1990), Molecular and eddy diffusion in the atmosphere of titan, *Ann. Geophys.*, *8*, 473–476.

Strobel, D. F., and D. E. Shemansky (1982), EUV emission from Titan's upper atmosphere: Voyager 1 encounter, *J. Geophys. Res.*, *87*, 1361–1368.

Strobel, D. F., R. R. Meier, M. E. Summers, and D. J. Strickland (1991), Nitrogen airglow sources: Comparison of Triton, Titan and Earth, *Geophys. Res. Lett.*, *18*, 689–692.

Strobel, D. F., M. E. Summers, and X. Zhu (1992), Titan's upper atmosphere: Structure and ultraviolet emissions, *Icarus*, *100*, 512–526.

Toublanc, D., J. P. Parisot, J. Brillet, D. Gautier, F. Raulin, and C. P. McKay (1995), Photochemical modeling of Titan's atmosphere, *Icarus*, *113*, 2–26.

Vervack, R. J., Jr., B. R. Sandel, and D. F. Strobel (2004), New perspectives on Titan's upper atmosphere from a reanalysis of the Voyager 1 UVS solar occultations, *Icarus*, *170*, 91–112.

Waite, J. H., Jr., et al. (2005a), The Cassini ion neutral mass spectrometer (INMS) investigation, *Space Sci. Rev.*, *114*, 113–231.

Waite, J. H., Jr., et al. (2005b), Ion neutral mass spectrometer results from the first flyby of Titan, *Science*, *308*, 982–986.

Wilson, E. H., and S. K. Atreya (2004), Current state of modeling the photochemistry of Titan's mutually dependent atmosphere and ionosphere, *J. Geophys. Res.*, *109*, E06002, doi:10.1029/2003JE002181.

Yelle, R. V., N. Borggren, V. De La Haye, W. T. Kasprzak, H. B. Niemann, I. Müller-Wodarg, and J. H. Waite Jr. (2006), The vertical structure of Titan's upper atmosphere from Cassini ion neutral mass spectrometer measurements, *Icarus*, *182*, 567–576.

Yung, Y. L., M. Allen, and J. P. Pinto (1984), Photochemistry of the atmosphere of Titan: Comparison between model and observations, *Astrophys. J. Suppl. Ser.*, *55*, 465.

T. E. Cravens and I. P. Robertson, Department of Physics and Astronomy, University of Kansas, Lawrence, KS 66045, USA.

V. De La Haye, D. A. Gell, B. Magee, and J. H. Waite Jr., Southwest Research Institute, 6220 Culebra, San Antonio, TX 78228, USA.

R. E. Johnson, Astronomy Department, University of Virginia, Charlottesville, VA 22904, USA.

S. Jurac, Center for Space Research, Massachusetts Institute of Technology, 77 Massachusetts Avenue, Cambridge, MA 02139, USA.

W. T. Kasprzak, NASA Goddard Space Flight Center, Greenbelt, MD 20771, USA.

F. Leblanc, Service d'Aéronomie du CNRS/IPSL, Jussieu, F-75252 Paris, France.

J. G. Luhmann, Space Sciences Laboratory, University of California, Berkeley, CA 94720, USA.

M. Michael, Civil Engineering CC-220, Indian Institute of Technology, Kanpur 208016, India.

R. V. Yelle, Lunar and Planetary Laboratory, University of Arizona, Tucson, AZ 85721, USA.